Driving electrochemical organic hydrogenations on metal catalysts by tailoring hydrogen surface coverages

Tengfei Li[1], Anna Ciotti[2], Motiar Rahaman[1], Celine Wing See Yeung[1], Max García-Melchor[2*], Erwin Reisner[1*]

[1]Yusuf Hamied Department of Chemistry, University of Cambridge, Lensfield Road, Cambridge CB2 1EW, United Kingdom.

[2]School of Chemistry, CRANN and AMBER Research Centres, Trinity College Dublin, College Green, Dublin2, Ireland

*Corresponding authors. Email: garciamm@tcd.ie ; reisner@ch.cam.ac.uk

Abstract: Electrochemical hydrogenation using renewable electricity holds promise as a sustainable approach to organic synthesis and the valorization of biomass-derived chemicals. Current strategies in the field usually employ alkaline conditions to suppress the competing hydrogen evolution reaction, and sourcing of hydrogen atoms for the hydrogenation is thus a challenge that can be addressed through local water dissociation on the electrode surface. Herein we demonstrate the computationally-guided design of electrochemical hydrogenation catalysts by tailoring their hydrogen coverage density and binding strength. Theoretical studies predict Cu, Au and Ag (with moderate H coverages) to be promising catalysts for electrochemical hydrogenation in alkaline media, which experiments confirm for a model organic substrate attaining yields and Faradaic efficiencies up to 90%. Furthermore, Cu, a non-precious metal electrocatalyst, is shown to promote the selective hydrogenation of a broad scope of unsaturated compounds featuring C=O, C=C, C≡C, and C≡N bonds with moderate to excellent conversions and chemoselectivities. Overall, this work demonstrates how the hydrogen coverage on the electrode surface can be tailored to design electrocatalysts based on non-precious metals for the hydrogenation of organic substrates. This knowledge is envisioned to guide the development of more efficient catalysts for organic hydrogenations as well as other chemical transformations of industrial interest.

Introduction

The anthropogenic emissions of CO_2 since the industrial revolution, in part by numerous industrial chemical processes that rely on reagents produced from fossil fuels, has already left an enduring effect on the Earth's environment and climate.(*1*) Defossilization of our economy can be supported through the electrification of industrial synthetic processes by coupling electrosynthesis with renewable energy sources.(*2-6*) For example, electrochemical hydrogenation (ECH) of organic substrates has emerged as a promising strategy to synthesize organics and valorize biomass derivatives to produce valuable fine chemicals, natural products, and medicines.(*7-11*) Furthermore, if driven by renewable electricity under mild conditions, ECH could supersede traditional thermal hydrogenation processes, which typically demand highly pure H_2 produced from steam reforming, as well as high pressures and elevated temperatures.(*12-14*)

Organic ECH reactions for a series of functional groups have been reported, including C=O, C=C, C≡C and C≡N (**Fig 1A**).(*15-28*) However, these systems typically rely on precious metal catalysts, such as Pt and Pd.(*22, 29, 30*) Moreover, in aqueous media, these cathode materials face the competition with the more facile hydrogen evolution reaction (HER), which usually requires less negative potentials, compromising the Faradaic efficiency (FE) towards the target ECH products. One strategy to minimize the competing HER is to work in alkaline media, wherein the concentration of protons is much lower.(*31*) A notable example is the ECH of acetonitrile, where a FE of 80-90% was achieved at 100-500 mA cm^{-2} in 1 M aqueous NaOH, in contrast to the dominant HER under acidic or neutral conditions.(*18*)

While hindering HER to the advantage of ECH reactions, the use of alkaline electrolytes poses important requirements due to the change in the sourcing hydrogen under these conditions: ECH sources H atoms from protons present in the acidic electrolyte, whereas H atoms are mainly sourced through water dissociation on the electrode surface in alkaline solution (**Fig 1B**).(*32*) In addition, the adsorbed H atoms must exhibit a moderate binding strength at the operating applied potential in order to facilitate the ECH of the organic substrate, according to the Sabatier's principle.(*33*) Hence, we envisioned the presence of a surface coverage of moderately bound H atoms to be crucial to effectively promote ECH in alkaline media while minimizing the competing HER.

Recent computational studies have proven valuable in rationalizing the ECH of organic compounds on Pd systems based on the binding of key reaction intermediates.(*24, 25*) However, to the best of our knowledge, the influence of the electrode surface coverage on the ECH activity/selectivity has not yet been reported in the literature. We believe this knowledge is critical to rationally design high-performance ECH electrocatalysts based on earth-abundant elements, which explains why such materials have remained elusive.

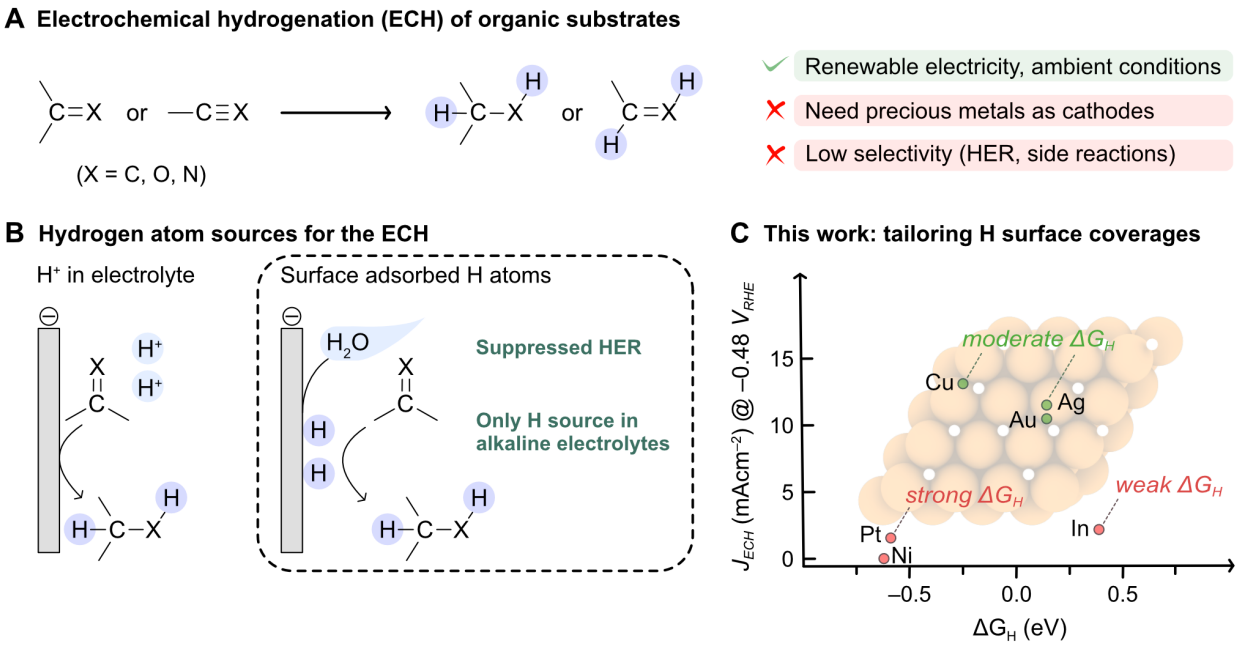

Fig 1. ECH of organic substrates. (**A**) Previous reports on ECH of organic compounds. (**B**) Illustration of the H source for ECH in acidic and alkaline media. (**C**) Schematic illustration of ECH driven by tailoring the hydrogen surface coverage, as reported in this work. The y-axis represents the partial current density towards ECH (J_{ECH}) and the x-axis the Gibbs adsorption energy of hydrogen (ΔG_H). Inset: an example of a metal cathode surface with 75% of the *fcc* sites covered by H atoms.

Herein, we report a bottom-up approach for designing non-precious metal cathodes for the selective ECH of organic substrates. Computational investigations of the density and binding strength of H surface coverages on different transition metals under relevant ECH conditions have identified Cu, Au, and Ag as promising electrocatalysts. These theoretical predictions are experimentally demonstrated for the ECH of acetophenone (AP) to 1-phenylethanol (1-PEA) on Ag, Au and Cu electrodes, achieving FEs and yields up to 90% at low applied potentials (*ca.* –0.5 V_{RHE}) and in alkaline media. Notably, these cathodes outperform other transition metals tested in this work by at least one order of magnitude in terms of FEs and yields, including In, Ni, and even the precious Pt metal, which is deemed as a state-of-the-art ECH electrocatalyst (**Fig. 1C**).(*20, 21*) In addition, experimental studies show that this bottom-up approach may be generalized to other organic unsaturated substrates featuring C=O, C=C, C≡C, and C≡N bonds, obtaining remarkable yields (70-90%) from ECH on a Cu electrode. Overall, this work highlights the importance of H surface coverages in ECH processes and how this knowledge can be leveraged to tailor non-noble metal cathodes to sustainably produce chemical feedstocks and added-value products.

Metal surface coverages under ECH conditions

While alkaline electrolysis can minimize the competing HER, the electrode surface under these conditions might still be able to dissociate water to source the H atoms needed for ECH. Therefore, we posited that an ideal ECH catalyst should promote water dissociation in an alkaline media, retaining the H atoms as distant as possible to minimize HER and with moderate binding strength to facilitate the ECH of organic substrates. To identify cathode materials that satisfy these premises, we performed periodic density functional theory (DFT) calculations on several transition metals, namely Ag, Au, Cu, Ni, and In (see details in Supplementary Materials). These elements were chosen as they display a wide range of H binding energies at reducing potentials based on previous theoretical studies on HER.(*34*) For comparison, we also included Pt in our investigations as it is regarded as a state-of-the-art ECH electrocatalyst.(*20, 21*) For each metal, the relative Gibbs adsorption energies (ΔG_i) of different surface terminations with varying concentrations of *H, *OH, and *O species (* denotes a surface metal site) were investigated as a function of the applied potential. The results of this analysis are illustrated in the surface diagrams depicted in **Fig. 2**, which reveal that *OH and *O coverages (orange/red lines) are favored at positive (oxidizing) potentials, while *H coverages (blue lines) are favored at negative (reducing) potentials, as expected. Accordingly, in the potential window commonly used in ECH studies (*i.e.* from 0 to –1.0 V_{RHE}), we predict the metals to present different concentrations of adsorbed H atoms. We also note that the calculated ΔG_H (in eV) at 0 V_{RHE} for one H atom adsorbed on the different metals follows the trend: In (+0.90) > Ag (+0.64) ~ Au (+0.64) > Cu (+0.25) > Ni (–0.12) ~ Pt (–0.09). These values, besides being a good description for the HER,(*35*) can be taken as an indication of the thermodynamic driving force towards water dissociation.(*32, 35*) More specifically, very positive values of ΔG_H imply a lack of surface H atoms available for ECH (*e.g.* In displays the highest ΔG_H value, and therefore its surface is predicted to be bare), whereas negative values are expected to favor water dissociation, although they may also hinder ECH since the H transfer to the substrate would become energetically demanding.(*32*) In light of these computational data, and the fact that ΔG_H shifts by $-eU$ with the applied potential U according to the computational hydrogen electrode model,(*36*) we hypothesized Cu, Ag and Au to be good candidates to promote the ECH of organic substrates in alkaline media at relatively low potentials by sourcing H atoms from the surface coverage.

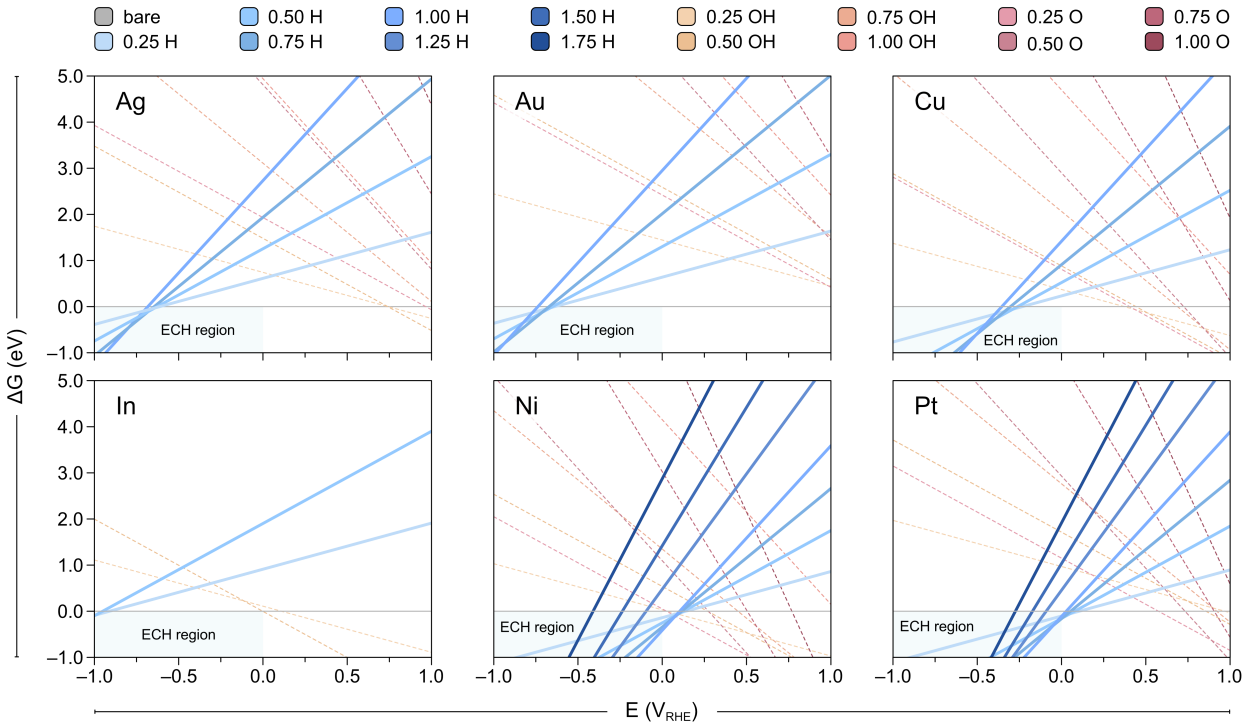

Fig. 2. Surface coverage analysis of Ag, Au, Cu, Ni, In, and Pt metal cathodes. Plots represent relative Gibbs energies of surface terminations with varying concentrations of adsorbed *H, *OH, and *O species (* denotes a metal surface site) as a function of applied potential, *E*. The dashed lines in red and orange represent *OH and *O coverages, while thick lines in blue denote *H coverages and the grey line is the bare surface. Darker colors correspond to higher coverage densities. The region of coverages relevant for the ECH is highlighted in light blue. All the metals were modelled as (111) surface slabs with *p*(2×2) periodicity, except In which was modelled as a (101) slab. Different colors and labels denote the relative concentration of adsorbed species in each surface termination, with darker colors corresponding to higher densities. Since all the (2×2) supercells contain four surface sites of each type (*i.e. bridge*, *fcc*, *hcp* and *top*), the fraction of occupied sites varies by multiples of 0.25 (*e.g.* 0.25 H denotes a quarter of the *fcc* sites covered by H atoms, 0.50 H half of the *fcc* sites covered by H atoms, etc.). For further details, see Supplementary Materials.

ECH of acetophenone on different metal cathodes

Next, we performed ECH experiments to validate the trends predicted by theoretical studies. For this, AP was chosen as a model substrate because: (i) the C=O group is activated by the aromatic structure; and (ii) the hydrogenation of AP is the most common route of producing 1-PEA (**Fig. 3A**), an important precursor in pharmaceutical and fragrance industries.(*37*) Among the metal cathodes investigated in this work, Cu was first studied to drive the ECH of AP, as it was predicted to be one of the most active ones by DFT calculations. The Cu electrocatalyst was prepared by an electrodeposition method following a previously reported protocol (see Supplementary Materials).(*38*) Scanning electron microscopy (SEM) analysis showed a porous dendritic

morphology (Supplementary Figure S1) of the Cu catalyst, whereas X-ray diffraction (XRD) analysis showed the crystal planes of the Cu catalyst (Supplementary Figure S2).

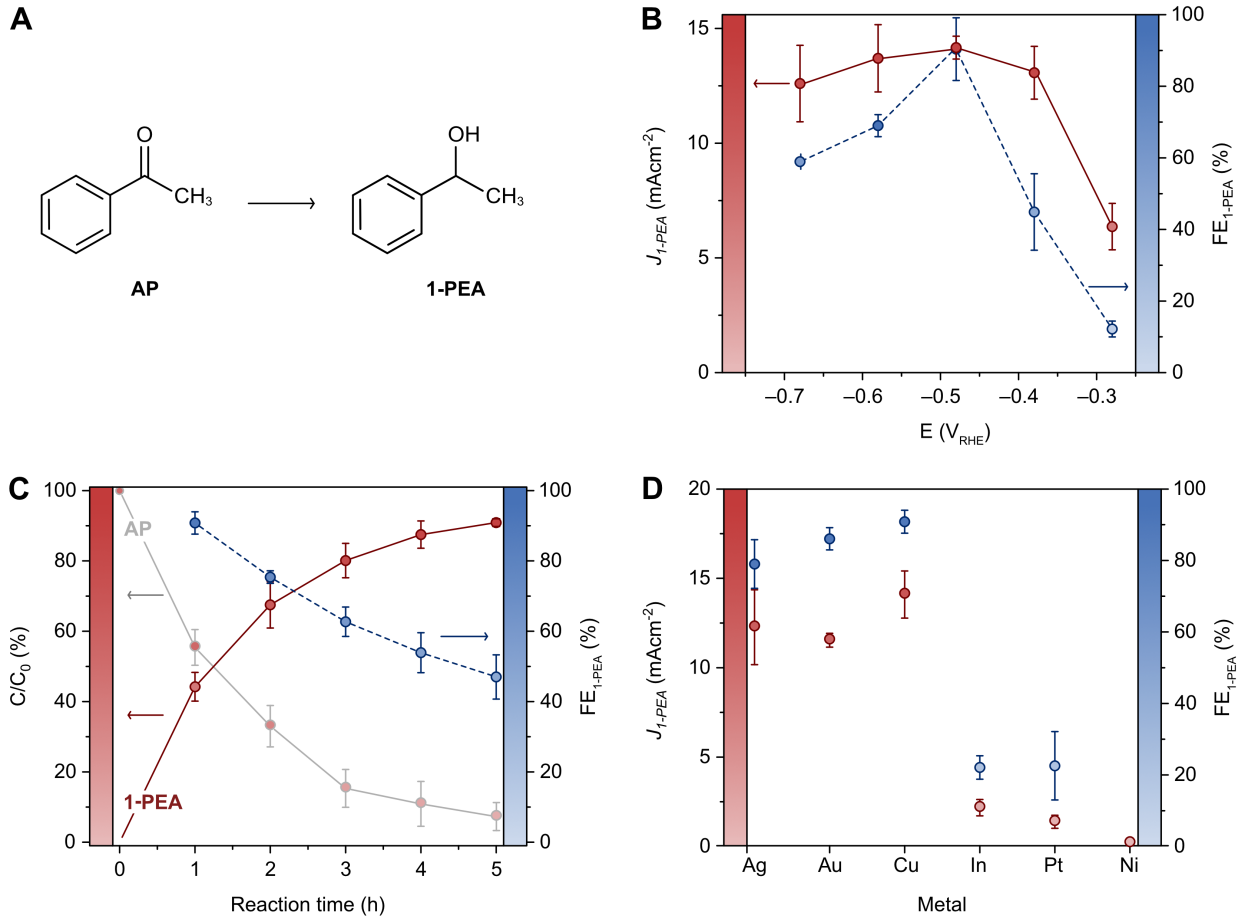

Fig. 3. ECH of AP to 1-PEA. (**A**) Schematic reaction of the hydrogenation of AP to 1-PEA. (**B**) $J_{1\text{-PEA}}$ (red, solid line) and $FE_{1\text{-PEA}}$ (blue, dashed line) for the ECH of AP to 1-PEA measured on the Cu electrocatalyst at potentials between –0.28 and –0.68 V_{RHE} after 1 h electrolysis. (**C**) Concentration profile of products (red, solid line) and reactants (grey, solid line), and $FE_{1\text{-PEA}}$ (blue, dashed line) for the ECH of AP on the Cu electrocatalyst over 5h electrolysis at –0.48 V_{RHE}. Concentrations of reactants/products were quantified by ^{1}H-NMR. (**D**) $J_{1\text{-PEA}}$ (red) and $FE_{1\text{-PEA}}$ (blue) measured for the ECH of AP to 1-PEA on Ag, Au, Cu, In, Pt and Ni electrocatalysts at –0.48 V_{RHE} after 1 h electrolysis. Error bars correspond to the standard deviation of triplicate experiments.

Electrochemistry experiments were performed in aqueous potassium phosphate buffer solution (pH = 11.8). Details of the experimental setup can be found in the Supplementary Materials. Cyclic voltammograms (CVs) collected on the Cu electrocatalyst (Supplementary Figure S4) revealed a significant increase in current density upon the addition of AP into the electrolyte solution, indicating the ability of Cu to promote ECH. Chronoamperometry experiments were then conducted within a potential window of –0.28 and –0.68 V_{RHE}, and the reaction mixture was

analyzed by proton nuclear magnetic resonance (^{1}H-NMR) spectroscopy after 1 h to quantify the yield of 1-PEA. The FE and partial current density towards 1-PEA ($FE_{1\text{-}PEA}$ and $J_{1\text{-}PEA}$, respectively) are shown in **Fig. 3B**. A $FE_{1\text{-}PEA}$ of 41±6% and $J_{1\text{-}PEA}$ of 1.9±0.4 mA cm^{-2} were observed at –0.28 V_{RHE}, which increased with more reducing potentials, reaching maximum values of 91±3% and 14±1 mA cm^{-2}, respectively, at –0.48 V_{RHE}. The remaining product was confirmed to be H_2 by gas chromatography. The $FE_{1\text{-}PEA}$ and $J_{1\text{-}PEA}$ started to decrease at higher potentials, between –0.58 and –0.68 V_{RHE}. Optimization of the electrolyte pH and Cu catalyst deposition time is shown in Supplementary Figure S5, which reveals an optimal pH of 11.8 and a deposition time of 40 s.

Figure 3C shows the results from controlled potential electrolysis of AP at –0.48 V_{RHE} over 5 h under stirring (10 mL of solution containing 0.5 mmol AP, electrode surface area = 0.84 cm^2), where the reaction mixture was analyzed by ^{1}H-NMR spectroscopy (Supplementary Figure S6) every hour to quantify the amounts of AP and 1-PEA in the solution. After 5 h, a yield of 91±1% was achieved for 1-PEA, and the AP remaining in the electrolyte solution was only 7.3±4%. The $FE_{1\text{-}PEA}$ was higher than 60% in the first 3 h of electrolysis, and still maintained at 47±6% when the conversion was finished after 5 h. The ECH of AP was also investigated on Ag, Au, In, Pt and Ni electrocatalysts (Supplementary Figure S7 shows the morphologies) at –0.48 V_{RHE} for 1 h (**Fig. 3D**). Ag and Au exhibited high $FE_{1\text{-}PEA}$ (80-90%) and $J_{1\text{-}PEA}$ (10-15 mA cm^{-2}) values, whereas In and Pt showed much lower performances (*i.e.* $FE_{1\text{-}PEA}$ ~20% and $J_{1\text{-}PEA}$ ~2.5 mA cm^{-2}) and Ni did not show any ECH activity. These results collectively demonstrate the efficient ECH of AP to 1-PEA on Cu, Ag and Au, as predicted by computational surface coverage studies.

ECH mechanistic studies

To further shed light on the reactivity trend observed in experiments, we next investigated the reaction mechanism for the ECH of AP to 1-PEA on the different metal cathodes by DFT calculations. Given that the pK_a of the mono-hydrogenated form of AP (APH·) is reported to be of 9.9 in water,(*39*) we deemed the non-hydrogenated form of AP to dominate in solution at the working pH of 11.8. Hence, we assumed that the H atoms required for ECH must be primarily sourced from the H surface coverage, if present. As discussed above, DFT calculations predict the In surface to be bare under reaction conditions. Hence, we rationalize the poor ECH activity on this metal with the lack of surface H atoms, and no further mechanistic investigations were conducted for this cathode. For the rest of the metals, the ECH mechanism was explored on the surface coverages predicted in **Fig. 2**. This corresponds to 25% of the *fcc* sites covered by H (0.25 H) on Ag and Au, 75% for Cu (0.75 H), and 100% for Ni and Pt (1.00 H), as shown in **Fig. 4A**.

The lowest energy ECH mechanism (see Supplementary Materials for details), depicted in **Fig. 4B**, begins with the adsorption of AP on the different metal coverages, which lies parallel to the surface at *ca.* 3.5-4 Å, interacting through the π-system. Because of the physisorbed nature of this intermediate (*AP, **Fig. 4C**), the range of the calculated binding energies is very narrow, *i.e.* from –0.01 (Ag) to 0.14 (Cu) eV (**Fig. 4B**), and therefore, the binding energy of *AP cannot be taken

as a good descriptor for the ECH process. Hence, we next modelled the hydrogenation of *AP, which can occur either at the C or O atoms of the carbonyl group. According to simulations, the hydrogenation at the O is thermodynamically more favorable on all the metals except Ag and Cu, which favor the hydrogenation at the C (see Supplementary Materials). This latter mechanism, however, is hindered by an energy barrier of *ca.* +2.0 eV (Supplementary Figure S8), rendering this pathway very unlikely at ambient experimental conditions.

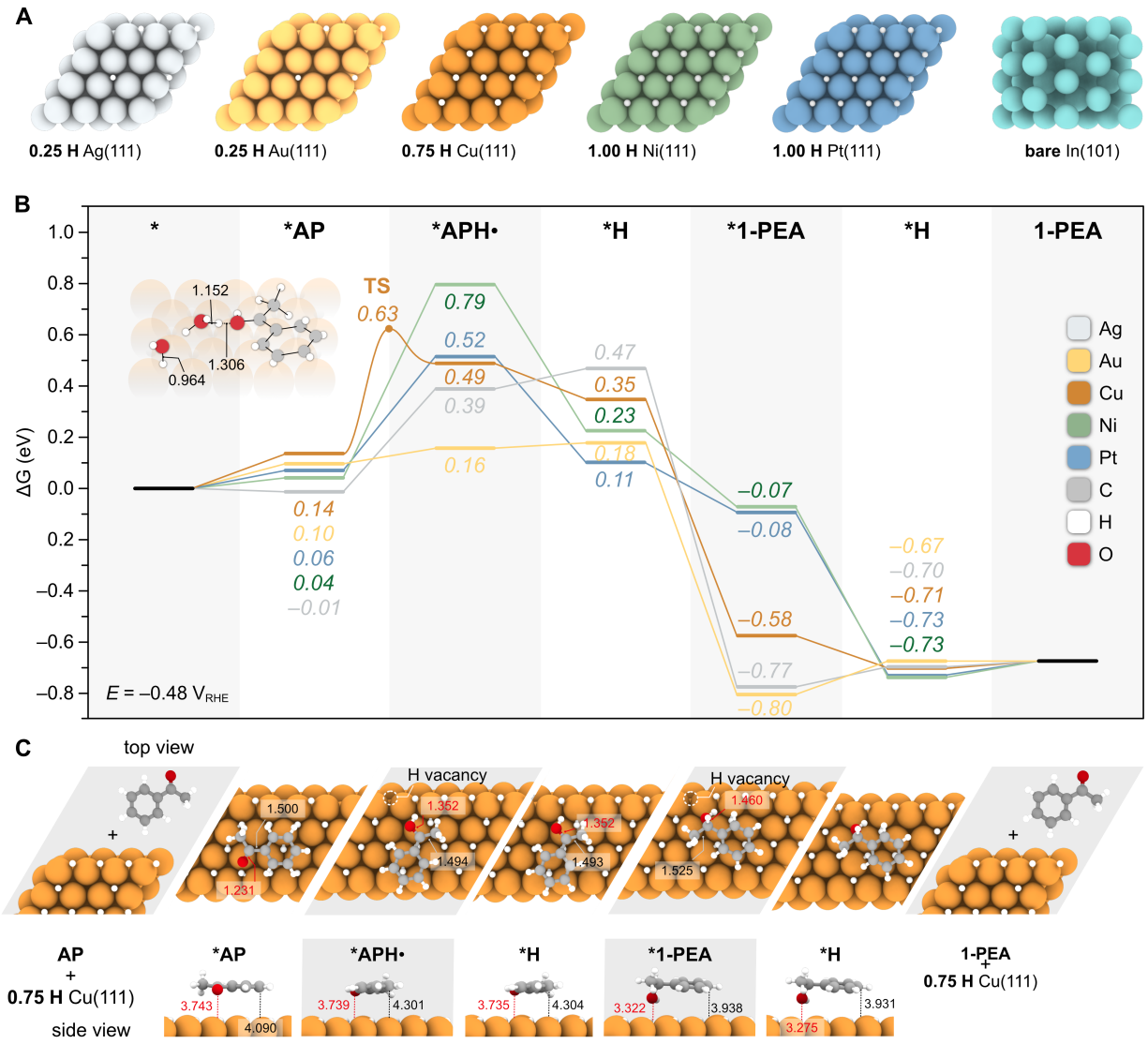

Fig. 4. ECH mechanistic studies on the different metal cathodes. (**A**) Resting states of the Ag, Au, Cu, Ni, Pt and In metal cathodes under ECH conditions based on the surface coverage analysis shown in Fig. 2. (**B**) Gibbs energy profile for the ECH of AP to 1-PEA calculated at the experimental potential of –0.48 V_{RHE}. The ECH mechanism involves AP adsorption (*AP), hydrogenation at the O atom (*APH·), refilling of the H vacancy left in the surface coverage (*H), hydrogenation at the C atom (*1-PEA), refilling of the H vacancy (*H), and product desorption (1-PEA). The optimized transition state structure for the first hydrogenation step assisted by two

water molecules on the diffused 0.75 H coverage of Cu(111) is shown in the inset. (**C**) Top and side view representations of the optimized structures of the main reaction intermediates *AP, *APH·, *H, and *1-PEA on Cu(111). Relevant bond distances (in Å) involving C and O atoms are shown in grey and red, respectively.

On the other hand, the hydrogenation of the carbonyl O in *AP leads to the intermediate *APH·. This species has a radical character delocalized over the aromatic ring, as confirmed by the magnetic moments obtained in the DFT simulations (see Supplementary Materials), which contributes to lower the energy of this intermediate. Interestingly, this second step is endergonic on all the investigated metals, *i.e.* Au (+0.16) < Ag (+0.39) < Cu (+0.49) < Pt (+0.52) < Ni (+0.79) (**Fig. 4B**), and correlates well with the respective ΔG_H values obtained in the surface coverage analysis shown in **Fig. 2**. Specifically, the formation of *APH· becomes less favorable with more negative values of ΔG_H, as we envisioned for ECH catalysts operating in alkaline media. Once *APH· is formed, the H surface vacancy is regenerated (*H), followed by the hydrogenation at the C atom to yield the final product, *1-PEA. This step is highly exergonic on all the cathodes, *i.e.* Au (–0.80) < Ag (–0.77) < Cu (–0.58) < Pt (–0.08) < Ni (–0.07) (**Fig. 4B**). Finally, the H coverage is regenerated (*H) again, and 1-PEA desorbs from the metal surface, closing the catalytic cycle.

Overall, DFT calculations reveal that the ECH of AP to 1-PEA is thermodynamically downhill on all the investigated metals under the experimental conditions of this work, and that the most endergonic step in the reaction mechanism is the first hydrogenation to yield *APH·. More specifically, Ni displays the most endergonic hydrogenation towards *APH·, which together with the competing HER explains the very poor ECH performance observed in experiments with this cathode. In the case of Pt, the energy landscape for ECH is feasible at ambient conditions, so we attribute its poor activity to the very strong competition with HER.(*20, 21*) Lastly, Au, Ag, and Cu exhibit the most favorable energetics (**Fig 4B**), in agreement with experimental observations. Additionally, upon H diffusion, which is reported to be facile on *fcc* metal surfaces,(*40*) we find that $\Delta G_{*APH\cdot}$ on the 0.75 H coverage on Cu is further lowered from +0.49 to +0.39 eV, while no marked improvement is observed on the less dense 0.25 H coverage (see Supplementary Materials). To provide a more detailed understanding of the ECH mechanism on these three electrodes, as well as the potential role of the water solvent in aiding the transfer of adsorbed H atoms, we set out to investigate the reaction kinetics of the most endergonic step (*AP → *APH·) on the 0.25 H coverage of Ag and Au, and on the diffused 0.75 H coverage of Cu. With this aim, the corresponding transition states (TS) connecting the adsorbed *AP and *APH· intermediates were modelled both in the gas phase and in the presence of up to three explicit H_2O molecules. Notably, we observe that the calculated energy barriers significantly decrease with the introduction of two waters, which act as a proton shuttle between the metal surface and the physisorbed *AP (inset, **Fig. 4B**), while no marked improvement is observed with the addition of the third (see Supplementary Figure S8). In particular, the energy barriers decrease by *ca.* +1.5 eV in the presence of two waters with respect to the calculations in vacuum, highlighting the critical role of

the water solvent in promoting ECH. Furthermore, these barriers assisted by two waters, calculated relative to the lowest energy intermediate preceding the TS, are coherent with ECH activity at ambient conditions, *i.e.* Au (+0.30) < Cu (+0.63) < Ag (+1.02). However, neither the predicted thermodynamic $\Delta G_{*APH\cdot}$ values (Au < Ag ~ Cu), nor the kinetic barriers for *AP hydrogenation (Au < Cu < Ag) alone, can fully explain the experimental trends of $J_{1\text{-}PEA}$ (Cu > Ag ~ Au). We rationalize this with the fact that, under reaction conditions, the 0.25 H coverages on Ag and Au are predicted to be in equilibrium with the bare surface, which is deemed to be inactive (**Fig. 2**). On the other hand, the 0.50 H, 0.75 H, and 1.0 H coverages on Cu exhibit similar stabilities and comparable ECH activities according to their associated $\Delta G_{*APH\cdot}$ values and the calculated barrier for *AP hydrogenation (see Supplementary Figure S8). Altogether, the fact that the most stable coverages of Cu under reaction conditions are deemed to be active towards ECH, while the predicted coverages for Ag and Au are in equilibrium with the inactive bare surface, is consistent with the activity trend observed in experiments. These thermodynamic and kinetic investigations of the different metal surfaces therefore confirm our initial hypothesis on the requirements to promote ECH in alkaline conditions. More specifically, ECH catalysts must promote water dissociation and reduce the generated protons to H atoms while retaining them on the surface with moderate strength to facilitate ECH. The adsorbed hydrogens should also be spaced out on the electrode surface to prevent HER via a Volmer-Heyrovsky mechanism. Finally, our findings also reveal that surface H diffusion can increase the binding of key reaction intermediates, highlighting the importance of the H surface coverage in ECH, as well as its dynamics.

Based on the very promising results described above, we envisioned that the H surface coverage of metal cathodes could be tailored to promote other ECH reactions, provided that the experiments are performed at pH values higher than the pK_a of the hydrogenated organic substrate, so that the H atoms needed for ECH must be sourced through H_2O dissociation on the electrode surface.

ECH of different organic substrates on the Cu catalyst

After confirming Cu as one of the most active electrocatalysts for AP reduction, we set out to broaden the substrate scope of ECH reactions that can be driven by this metal (**Fig. 5**). Following the ECH of a ketone such as AP, we next investigated the ECH of benzaldehyde as an example of aldehyde hydrogenation. Adopting the same reaction conditions (*i.e.* –0.48 V_{RHE}, pH = 11.8), benzaldehyde was converted into benzyl alcohol on a Cu cathode with a yield of 85% after 3 h electrolysis (**Fig. 5A**). Details of the NMR spectra and temporary changes of concentrations can be found in the Supplementary Figures S9 and S10.

Next, we explored the possibility of hydrogenating the C=C double bond in maleic acid (**Fig. 5B**). This process is an important strategy to upgrade the biomass-derived maleic acid into succinic acid (SA), a valuable chemical feedstock which can be used as polymer precursor, food addictive and dietary supplement.(*41, 42*) The experimental conditions adopted for the ECH of maleic acid were the same as for AP, except for the electrolyte pH which was optimized to 7.7 instead of 11.8 (see Supplementary Figure S11). The recorded ^{1}H-NMR spectra of the reaction mixtures, and the measured FE_{SA} and J_{SA} after 1 h of electrolysis at different potentials between –0.28 and –0.68

V_{RHE} are shown in are shown in Supplementary Figures S12 and S13A, respectively. Similarly to AP, the maximum ECH activity was observed at –0.48 V_{RHE} (FE_{SA} = 75±4%, J_{SA} = 12±1 mA cm^{-2}). Furthermore, constant potential electrolysis at –0.48 V_{RHE} resulted in 89±3% conversion of maleic acid and 89±3% yield of succinic acid after 8 h of electrolysis (Supplementary Figure S13B).

The ECH of maleic acid showed that it is possible to selectively hydrogenate C=C bonds by Cu. Therefore, we decided to investigate the selective ECH of the C=C in an α,β-unsaturated ketone, a challenging goal in organic electrosynthesis.(*12, 19*) With this aim, the ECH of cyclohex-2-en-1-one was explored under the same reaction conditions as for maleic acid, except the potential which was optimized to –0.58 V_{RHE}. After 1 h electrolysis, 24% of the reactant was converted, affording 22% of the desired C=C hydrogenation product (*i.e.* cyclohexanone) and only *ca.* 1% of the further hydrogenated product (*i.e.* cyclohexanol; see NMR spectra in Supplementary Figure S14). After 6 h of electrolysis, a remarkable conversion of 88% was achieved, split into 77% yield of cyclohexanone and 10% yield of cyclohexanol (**Fig. 5B** and Supplementary Figure S15). Hence, these results demonstrate the excellent chemoselectivity of this ECH process. We speculate that the extended d orbitals present in copper allow for an effective soft-soft interaction with the C=C π-bond selectively hydrogenating the olefin in α,β-unsaturated ketones whilst preserving the harder carbonyl groups.

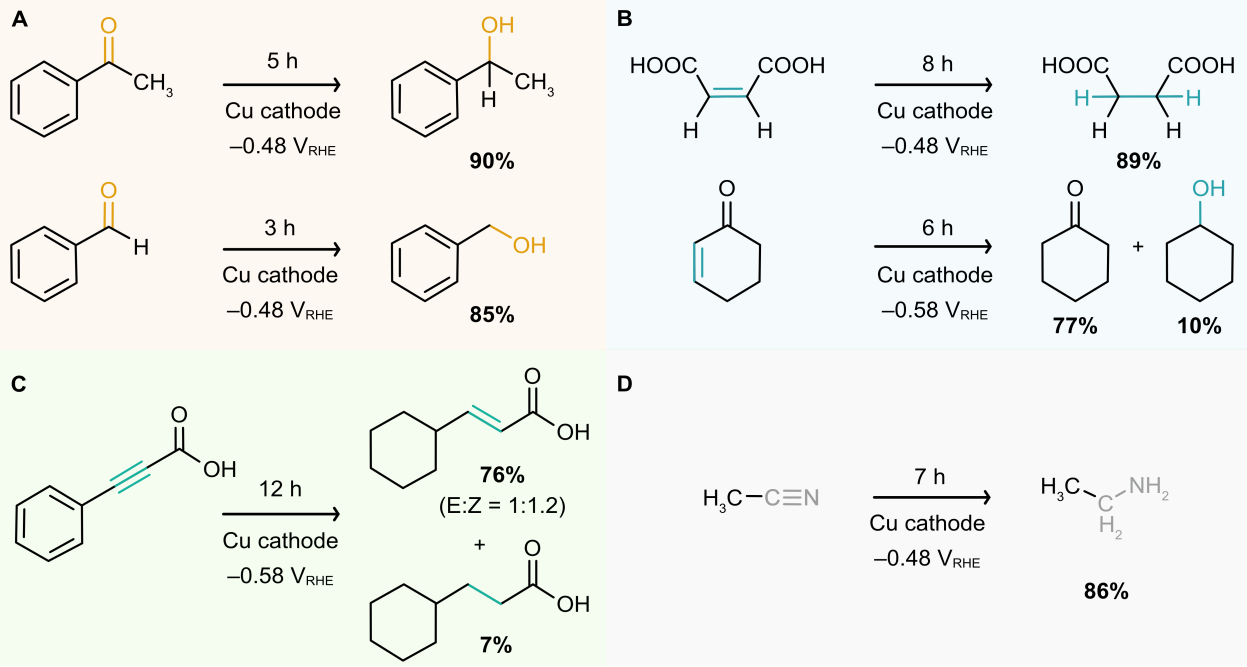

Fig. 5. ECH of different organic functional groups on a Cu cathode. (**A**) ECH of the C=O group in AP (ketone) and benzaldehyde (aldehyde). (**B**) ECH of the C=C group in maleic acid and cyclohex-2-en-1-one. (**C**) ECH of the C≡C group in phenylpropiolic acid. (**D**) ECH of the C≡N group in acetonitrile. Yields (%) provided were quantified by ^{1}H-NMR spectroscopy. The reaction time was optimized to achieve maximum yield of product.

The substrate scope on the Cu electrocatalyst was further extended to the ECH of C≡C triple bonds, namely the hydrogenation of phenylpropiolic acid (**Fig. 5C**. NMR spectra and temporary changes of concentrations can be found in Supplementary Figures S16-S17). The selective hydrogenation of C≡C to C=C (instead of the complete hydrogenation to C–C) is a major challenge in alkyne reduction in general.(*17*) Importantly, after 2 h of controlled potential electrolysis, 24% of the alkyne was converted into 21% of the corresponding alkene (*i.e.* cinnamic acid) and only *ca.* 0.5% of the alkane product (*i.e.* phenylpropanoic acid), while after 12 h, a total conversion of 82% was achieved with 76% and 7% of the alkene (a mixture of E/Z products) and alkane products, respectively. While excellent selectivities have been reported for the ECH of acetylene using a LDH-derived Cu catalyst(*17*) and electrochemically deposited Cu dendrites, our findings show both remarkable selectivity and chemoselectivity.

Finally, the ECH of C≡N triple bonds was studied using acetonitrile as a model substrate, since this is an interesting reaction to upgrade the excess acetonitrile manufacturing capacity to make value-added ethyl amine.(*18*) Notably, acetonitrile was hydrogenated into ethylamine with an overall yield of 86% after 7 h of electrolysis under similar reaction conditions (**Fig. 5D**, Supplementary Figures S18 and S19), demonstrating the broad scope of organic functional groups that can be hydrogenated on a Cu electrocatalyst, coherently with the computational predictions.

In summary, this work reports the computationally-guided design of non-precious metals for the selective ECH of unsaturated organic substrates in alkaline media. This is achieved by tailoring the density and binding strength of H coverages on the electrode surface and by establishing a series of catalyst design principles. In particular, metal cathodes are chosen to promote water dissociation and reduce the generated protons to H atoms, while retaining them on the electrode surface with moderate strength to facilitate ECH. In addition, metals displaying well-dispersed H atoms on the surface are desirable to prevent HER via a Volmer-Heyrovsky mechanism. With these premises, DFT calculations identify Cu, Au, and Ag as promising ECH electrocatalysts. Experimental studies confirm the excellent performance of these metals for the selective ECH of acetophenone (AP) to 1-phenylethanol (1-PEA) in alkaline media, attaining FEs and yields up to 90% at *ca.* –0.5 V_{RHE}. Notably, these cathodes outperform other transition metals investigated in this work by at least one order of magnitude in terms of FEs and yields, including In, Ni, as well as the state-of-the-art and precious Pt metal. This novel bottom-up approach of tailoring H surface coverages is further demonstrated with the successful ECH of a broad scope of unsaturated organics featuring C=O, C=C, C≡C, and C≡N bonds with moderate to excellent conversions and chemoselectivities (70-90%) on a Cu electrode. Overall, this work highlights the critical role of H surface coverages and how this knowledge can be leveraged to tailor high-performance ECH catalysts based on earth-abundant metals. Hence, this strategy is envisioned to pave the way for the rational design ECH catalysts to electrify the synthesis of chemical feedstocks and added-value products, thus contributing to reduce the carbon footprint of chemical industry.

Acknowledgments: T.L., M.R., C.W.S.Y. and E.R. thank the financial support from Canadian Banting Postdoctoral Fellowship, Marie Skłodowska-Curie Individual European Fellowship (SolarFUEL, GAN 839763), Singapore Agency for Science, Technology and Research

(A*STAR), and UKRI/ERC Advanced Grant (EP/X030563/1). A. C. and M. G.-M. gratefully acknowledge the financial support from the Science Foundation Ireland Research Centre Award under grant agreement number 12/RC/2278_P2. The authors also thank the DJEI/DES/SFI/HEA Irish Centre for High-End Computing (ICHEC) and the Supercomputing Laboratory at King Abdullah University of Science & Technology (KAUST) in Thuwal, Saudi Arabia, for the provision of computational resources. We also thank Dr. Arjun Vijeta (University of Cambridge) for useful input.

Author contributions: Methodology and Investigation: T.L. developed the ECH system; T.L. and W.S.C.Y. performed the electrochemical reactions; A.C. performed the theoretical calculations; M.R. designed, synthesized, and characterized the metal catalysts. Formal Analysis: T.L. analyzed the experimental results; A.C. and M.G.-M. designed the computational studies and analyzed the theoretical data; Funding acquisition/Supervision/Project Administration: M.G.-M. and E.R.; Writing: T.L., A.C., M.G.-M., and E.R. wrote the first draft. All authors contributed to the final draft.

Competing interests: Authors declare that they have no competing interests.

Data and materials availability: Computational data underlying this work, including cartesian coordinates and energies of the optimized structures are openly accessible in the following ioChem-BD dataset: https://doi.org/10.19061/iochem-bd-6-303. All data is available on repository (link to be added upon acceptance).

References and Notes

1. J. Barrett *et al.*, Energy demand reduction options for meeting national zero-emission targets in the United Kingdom. *Nat. Energy* **7**, 726-735 (2022).
2. P. De Luna *et al.*, What would it take for renewably powered electrosynthesis to displace petrochemical processes? *Science* **364**, eaav3506 (2019).
3. A. Wiebe *et al.*, Electrifying Organic Synthesis. *Angew. Chem. Int. Ed.* **57**, 5594-5619 (2018).
4. M. C. Leech, K. Lam, A practical guide to electrosynthesis. *Nat. Rev. Chem.* **6**, 275-286 (2022).
5. L. F. T. Novaes *et al.*, Electrocatalysis as an enabling technology for organic synthesis. *Chem. Soc. Rev.* **50**, 7941-8002 (2021).
6. T. Li *et al.*, Photoelectrochemical oxidation of organic substrates in organic media. *Nat. Commun.* **8**, 390 (2017).
7. J. F. E. Teichert, Homogeneous Hydrogenation with Non-Precious Catalysts. *Wiley-VCH, Weinheim*, 1-298 (2020).
8. S. A. Akhade *et al.*, Electrocatalytic Hydrogenation of Biomass-Derived Organics: A Review. *Chem. Rev.* **120**, 11370-11419 (2020).
9. H. U. Blaser *et al.*, Selective hydrogenation for fine chemicals: Recent trends and new developments. *Adv. Synth. Catal.* **345**, 103-151 (2003).
10. J. Yoshida, K. Kataoka, R. Horcajada, A. Nagaki, Modern strategies in electroorganic synthesis. *Chem. Rev.* **108**, 2265-2299 (2008).
11. M. Yan, Y. Kawamata, P. S. Baran, Synthetic Organic Electrochemical Methods Since 2000: On the Verge of a Renaissance. *Chem. Rev.* **117**, 13230-13319 (2017).

12. J. Mendes-Burak, B. Ghaffari, C. Coperet, Selective hydrogenation of α,β-unsaturated carbonyl compounds on silica-supported copper nanoparticle. *Chem. Commun.* **55**, 179-181 (2019).
13. P. J. Chirik, Iron- and Cobalt-Catalyzed Alkene Hydrogenation: Catalysis with Both Redox-Active and Strong Field Ligands. *Acc. Chem. Res.* **48**, 1687-1695 (2015).
14. L. Alig, M. Fritz, S. Schneider, First-Row Transition Metal (De)Hydrogenation Catalysis Based On Functional Pincer Ligands. *Chem. Rev.* **119**, 2681-2751 (2019).
15. Y. Kwon, Y. Y. Birdja, S. Raoufmoghaddam, M. T. M. Koper, Electrocatalytic Hydrogenation of 5-Hydroxymethylfurfural in Acidic Solution. *Chemsuschem* **8**, 1745-1751 (2015).
16. A. Kurimoto, R. S. Sherbo, Y. Cao, N. W. X. Loo, C. P. Berlinguette, Electrolytic deuteration of unsaturated bonds without using D_2. *Nat. Catal.* **3**, 719-726 (2020).
17. R. Shi *et al.*, Room-temperature electrochemical acetylene reduction to ethylene with high conversion and selectivity. *Nat. Catal.* **4**, 565-574 (2021).
18. R. Xia *et al.*, Electrochemical reduction of acetonitrile to ethylamine. *Nat. Commun.* **12**, (2021).
19. I. Fokin, I. Siewert, Chemoselective Electrochemical Hydrogenation of Ketones and Aldehydes with a Well-Defined Base-Metal Catalyst. *Chem-Eur J* **26**, 14137-14143 (2020).
20. C. J. Bondue, M. T. M. Koper, Electrochemical Reduction of the Carbonyl Functional Group: The Importance of Adsorption Geometry, Molecular Structure, and Electrode Surface Structure. *J. Am. Chem. Soc.* **141**, 12071-12078 (2019).
21. C. J. Bondue, F. Calle-Vallejo, M. C. Figueiredo, M. T. M. Koper, Structural principles to steer the selectivity of the electrocatalytic reduction of aliphatic ketones on platinum. *Nat. Catal.* **2**, 243-250 (2019).
22. R. S. Sherbo, R. S. Delima, V. A. Chiykowski, B. P. MacLeod, C. P. Berlinguette, Complete electron economy by pairing electrolysis with hydrogenation. *Nat. Catal.* **1**, 501-507 (2018).
23. M. Villalba, M. del Pozo, E. J. Calvo, Electrocatalytic hydrogenation of acetophenone and benzophenone using palladium electrodes. *Electrochim. Acta* **164**, 125-131 (2015).
24. D. C. Cantu *et al.*, A Combined Experimental and Theoretical Study on the Activity and Selectivity of the Electrocatalytic Hydrogenation of Aldehydes. *ACS. Catal.* **8**, 7645-7658 (2018).
25. J. A. Lopez-Ruiz *et al.*, Understanding the Role of Metal and Molecular Structure on the Electrocatalytic Hydrogenation of Oxygenated Organic Compounds. *ACS. Catal.* **9**, 9964-9972 (2019).
26. K. Obata *et al.*, Solar-driven upgrading of biomass by coupled hydrogenation using in situ (photo)electrochemically generated H2. *Nat. Commun.* **14**, 6017 (2023).
27. C. Russo *et al.*, eHydrogenation: Hydrogen-free Electrochemical Hydrogenation. *Angew. Chem. Int. Ed.* **62**, e202309563 (2023).
28. J. T. Kleinhaus *et al.*, Developing electrochemical hydrogenation towards industrial application. *Chem. Soc. Rev.*, (2023).
29. C. Han *et al.*, Electrocatalytic hydrogenation of alkenes with Pd/carbon nanotubes at an oil–water interface. *Nat. Catal.* **5**, 1110-1119 (2022).
30. U. Sanyal *et al.*, Hydrogen Bonding Enhances the Electrochemical Hydrogenation of Benzaldehyde in the Aqueous Phase. *Angew. Chem. Int. Ed.* **60**, 290-296 (2021).

31. N. Mahmood *et al.*, Electrocatalysts for Hydrogen Evolution in Alkaline Electrolytes: Mechanisms, Challenges, and Prospective Solutions. *Adv. Sci.* **5**, 1700464 (2018).
32. I. Ledezma-Yanez *et al.*, Interfacial water reorganization as a pH-dependent descriptor of the hydrogen evolution rate on platinum electrodes. *Nat. Energy* **2**, 17031 (2017).
33. H. Ooka, J. Huang, K. S. Exner, in *Frontiers in Energy Research*. (2021).
34. J. Greeley, T. F. Jaramillo, J. Bonde, I. Chorkendorff, J. K. Nørskov, Computational high-throughput screening of electrocatalytic materials for hydrogen evolution. *Nat. Mater.* **5**, 909-913 (2006).
35. Z. W. Seh *et al.*, Combining theory and experiment in electrocatalysis: Insights into materials design. *Science* **355**, eaad4998 (2017).
36. J. K. Nørskov *et al.*, Origin of the Overpotential for Oxygen Reduction at a Fuel-Cell Cathode. *The Journal of Physical Chemistry B* **108**, 17886-17892 (2004).
37. G. Mohammadi Ziarani, Z. Kheilkordi, F. Mohajer, Recent advances in the application of acetophenone in heterocyclic compounds synthesis. *Journal of the Iranian Chemical Society* **17**, 247-282 (2020).
38. M. Rahaman *et al.*, Selective CO production from aqueous CO2 using a Cu96In4 catalyst and its integration into a bias-free solar perovskite–BiVO4 tandem device. *Energ Environ. Sci.* **13**, 3536-3543 (2020).
39. E. Hayon, T. Ibata, N. N. Lichtin, M. Simic, Electron and hydrogen atom attachment to aromatic carbonyl compounds in aqueous solution. Absorption spectra and dissociation constants of ketyl radicals. *The Journal of Physical Chemistry* **76**, 2072-2078 (1972).
40. L. Kristinsdóttir, E. Skúlason, A systematic DFT study of hydrogen diffusion on transition metal surfaces. *Surf. Sci.* **606**, 1400-1404 (2012).
41. K. L. Ong *et al.*, in *Food Industry Wastes (Second Edition),* M. R. Kosseva, C. Webb, Eds. (Academic Press, 2020), pp. 255-273.
42. C. Xing *et al.*, Highly Selective Electrocatalytic Olefin Hydrogenation in Aqueous Solution. *Angew. Chem. Int. Ed.* **62**, e202310722 (2023).
43. J. Bu *et al.*, Selective electrocatalytic semihydrogenation of acetylene impurities for the production of polymer-grade ethylene. *Nat. Catal.* **4**, 557-564 (2021).